The Astrophysical Journal Letters, 818:L18 (6pp), 2016 February 10 doi:10.3847/2041-8205/818/1/L18

LOCAL INTERSTELLAR MAGNETIC FIELD DETERMINED FROM THE *INTERSTELLAR BOUNDARY EXPLORER* RIBBON

E. J. Zirnstein[1], J. Heerikhuisen[2], H. O. Funsten[3], G. Livadiotis[1], D. J. McComas[1,4], and N. V. Pogorelov[2]
[1] Southwest Research Institute, San Antonio, TX 78228, USA; ezirnstein@swri.edu
[2] Department of Space Science, University of Alabama in Huntsville, Huntsville, AL 35899, USA
[3] Los Alamos National Laboratory, Los Alamos, NM 87545, USA
[4] Department of Physics and Astronomy, University of Texas at San Antonio, San Antonio, TX 78249, USA
Received 2015 December 15; accepted 2016 January 25; published 2016 February 8

ABSTRACT

The solar wind emanating from the Sun interacts with the local interstellar medium (LISM), forming the heliosphere. Hydrogen energetic neutral atoms (ENAs) produced by the solar-interstellar interaction carry important information about plasma properties from the boundaries of the heliosphere, and are currently being measured by NASA's *Interstellar Boundary Explorer* (*IBEX*). *IBEX* observations show the existence of a "ribbon" of intense ENA emission projecting a circle on the celestial sphere that is centered near the local interstellar magnetic field (ISMF) vector. Here we show that the source of the *IBEX* ribbon as a function of ENA energy outside the heliosphere, uniquely coupled to the draping of the ISMF around the heliopause, can be used to precisely determine the magnitude ($2.93 \pm 0.08\,\mu$G) and direction ($227\overset{\circ}{.}28 \pm 0\overset{\circ}{.}69$, $34\overset{\circ}{.}62 \pm 0\overset{\circ}{.}45$ in ecliptic longitude and latitude) of the pristine ISMF far (~1000 AU) from the Sun. We find that the ISMF vector is offset from the ribbon center by $\sim 8\overset{\circ}{.}3$ toward the direction of motion of the heliosphere through the LISM, and their vectors form a plane that is consistent with the direction of deflected interstellar neutral hydrogen, thought to be controlled by the ISMF. Our results yield draped ISMF properties close to that observed by *Voyager 1*, the only spacecraft to directly measure the ISMF close to the heliosphere, and give predictions of the pristine ISMF that *Voyager 1* has yet to sample.

Key words: ISM: atoms – ISM: magnetic fields – solar wind – Sun: heliosphere

1. INTRODUCTION

As the solar wind (SW) plasma flows away from the Sun, it encounters the local interstellar medium (LISM), and through their interaction forms the heliosphere (Parker 1961). While the LISM plasma far from the heliosphere is relatively cold (~7500 K) (McComas et al. 2015), the presence of a suprathermal ion population of heliospheric origin outside the heliopause can significantly modify the structure of the nearby LISM (Zank et al. 2013). These ions, whose dynamics are governed by the perturbed interstellar magnetic field (ISMF, $\boldsymbol{B}$) draped around the heliosphere, can be neutralized by charge-exchange with neutral hydrogen atoms to produce energetic neutral atoms (ENAs), which can be observed from the inner heliosphere by NASA's *Interstellar Boundary Explorer* (*IBEX*; McComas et al. 2009a).

During its initial observations, *IBEX* revealed the unexpected existence of a narrow "ribbon" of intense ENA emission (McComas et al. 2009b). The ribbon intensity produces a circular shape on the celestial sphere, with a center aligned near the radial vector pointing toward (longitude, latitude) (λ, β) = (221°, 39°) in Sun-centered, ecliptic J2000 coordinates (Funsten et al. 2009b). Comparisons of these observations to three-dimensional (3D) models of the heliosphere indicated that the ribbon ENA emission corresponds to viewing directions ($\boldsymbol{r}$) approximately perpendicular to $\boldsymbol{B}$ such that $\boldsymbol{B}\cdot\boldsymbol{r} \sim 0$ (Schwadron et al. 2009b). In fact, the observed vector direction of the ribbon's center as viewed from the inner heliosphere was hypothesized to define the pristine (undisturbed by the presence of the heliosphere) ISMF vector, $\boldsymbol{B}_\infty$.

Thus, the emission of ENAs from outside the heliopause may be preferentially directed back toward Earth in directions approximately perpendicular to $\boldsymbol{B}$, a process believed to be responsible for the ribbon (McComas et al. 2009b; Heerikhuisen et al. 2010). This process has been extensively studied and explains many key features of the ribbon (Zirnstein et al. 2015). In fact, modeling this process allows one to constrain $\boldsymbol{B}_\infty$ by correlating the perturbed ISMF near the heliopause with the geometry of the ribbon flux in the sky. Several studies utilized 3D magneto-hydrodynamic (MHD) simulations of the heliosphere to estimate $\boldsymbol{B}_\infty$ by correlating the average radius and center of the circular ribbon with directions toward $\boldsymbol{B}\cdot\boldsymbol{r} = 0$ outside a simulated heliosphere (Grygorczuk et al. 2011; Strumik et al. 2011; Ben-Jaffel & Ratkiewicz 2012; Ratkiewicz et al. 2012; Ben-Jaffel et al. 2013), or by comparing to simulations of the ribbon flux (Heerikhuisen & Pogorelov 2011; Heerikhuisen et al. 2014). Results from these studies gave solutions of $|\boldsymbol{B}_\infty| \sim 2$–$4\,\mu$G (most between 2 and 3 μG), and vector direction $<15°$ from the ribbon center as viewed from the inner heliosphere.

The ENA flux map at each energy is uniquely constructed from ENAs originating from overlapping source regions in the outer heliosheath (Figure 1). Each map is a consequence of the same SW-LISM interaction, but uniquely represents ENAs emitted from different regions outside the heliosphere with spatially varying properties (e.g., $\boldsymbol{B}$). The suprathermal ion population extends farther into the LISM at higher energies, thus providing a unique spectral signature that is embedded in the ENA emission. Using $\boldsymbol{B}_\infty$ as a universal boundary condition, direct 3D simulations of the ribbon emission at each energy can be used to tightly constrain $\boldsymbol{B}_\infty$, an approach not attempted before.

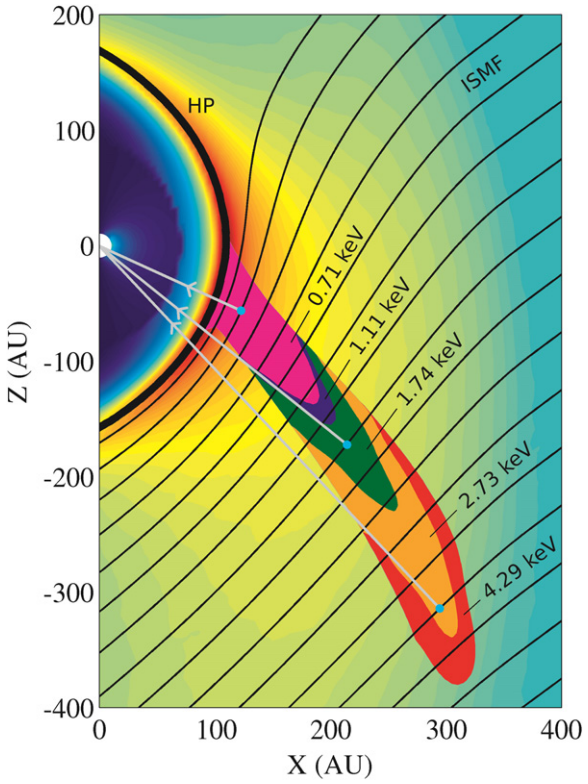

Figure 1. Isocontours of the ribbon ENA production rate outside the heliopause (HP) denoted by five colors distinguishing the ENA energies. The background color represents the magnetic field magnitude, with some ISMF lines (black curves). Suprathermal ions outside the HP become neutralized by charge-exchange (blue circles) and form ENAs that may travel back inward toward *IBEX* (gray lines). The majority of ribbon ENAs originate near $\boldsymbol{B}\cdot\boldsymbol{r}\sim 0$ (colored contours, only shown for $\cos^{-1}(\boldsymbol{B}\cdot\boldsymbol{r}) > 85°$). Due to the curvature of the ISMF and the finite temperature of parent ENAs, the ribbon source region is broad; however, the line of sight integrated flux decreases farther from $\boldsymbol{B}\cdot\boldsymbol{r} = 0$ (see Zirnstein et al. 2015).

2. METHOD OF SIMULATION

We utilize a 3D SW-LISM simulation that couples an MHD description of the solar and interstellar plasmas with a kinetic description of neutral hydrogen (Pogorelov et al. 2008b; Heerikhuisen & Pogorelov 2010). The MHD module solves the ideal MHD equations for a single fluid representing the SW and LISM plasmas. The MHD equations are coupled to the neutral hydrogen distribution through mass, momentum, and energy source terms via photo-ionization and charge-exchange. The kinetic module uses a Monte Carlo approach to solve the Boltzmann equation for the distribution of neutral hydrogen.

The SW boundary conditions at 1 AU are given by: plasma density $n_p = 5.74\,\mathrm{cm}^{-3}$, temperature $T_p = 51{,}100\,\mathrm{K}$, speed $v_p = 450\,\mathrm{km\,s}^{-1}$, and magnetic field radial component $B_r = 37.5\,\mu\mathrm{G}$. These conditions are then advected to the simulation inner boundary (10 AU) assuming adiabatic expansion. Neutral hydrogen atoms generated in the supersonic SW in the kinetic-neutral module are assigned velocities as a function of heliolatitude from SW speeds derived from an interplanetary scintillation observation-based model (Sokół et al. 2013; Zirnstein et al. 2013, 2015; Heerikhuisen et al. 2014), with a temperature spread derived from *Voyager* data.

While it is difficult to account for simulation uncertainties in our analysis, we attempt to minimize some. Our choice of SW temperature does not significantly affect the MHD solution since the flow is highly supersonic. To help eliminate an artificially flat current sheet and spurious magnetic reconnection at the heliopause due to numerical dissipation, the interplanetary magnetic field (IMF) is chosen to be monopolar with an orientation such that the IMF inside the heliopause near *Voyager 1 (V1)* is approximately parallel to the ISMF outside.

The LISM boundary conditions are shown in Table 1. The LISM densities are chosen in order to reproduce the distance to the heliopause in the *V1* direction, as well as to reproduce the interstellar neutral density at the nose of the termination shock (TS; Bzowski et al. 2009). Our simulation results do not reproduce the distances to the TS derived from *Voyager* (Stone et al. 2005, 2008), but this does not affect the position of the ribbon. Without self-consistent, time-dependent SW boundary conditions (Pogorelov et al. 2013) and a proper description of the IHS plasma (and thus a reduction of its thickness, see e.g., Malama et al. 2006; Izmodenov et al. 2014), it is nearly impossible to self-consistently reproduce the distances to the TS and heliopause simultaneously. For the purposes of simulating the ISMF draped around the heliosphere, it is more important to constrain the distance to the heliopause. Time-independent models using a strong ISMF ($|\boldsymbol{B}_\infty| > 4\,\mu$G) and smaller angle between $\boldsymbol{B}_\infty$ and $\boldsymbol{V}_\infty$ (15°–30°) were able to reproduce the *Voyager* crossing distances of the TS (Ratkiewicz & Grygorczuk 2008; Izmodenov et al. 2009; Opher et al. 2009), but these models did not reproduce the distance to the heliopause, and their ISMF parameters cannot reproduce the *IBEX* ribbon geometry and location (see Figure 2).

After simulating the SW-LISM interaction, we interpolate the plasma and neutral results in order to compute the probability for charge-exchange between the plasma and neutrals to create ENAs that will be detected at 1 AU. We simulate the ribbon flux at each *IBEX*-Hi energy using the *IBEX*-Hi energy responses (Funsten et al. 2009a; Schwadron et al. 2009a). For more details, see Zirnstein et al. (2013).

We determine the direction of $\boldsymbol{B}_\infty$ for $2\,\mu\mathrm{G} \leqslant |\boldsymbol{B}_\infty| \leqslant 4\,\mu\mathrm{G}$ by requiring that the location of the simulated ribbon's center projected in the sky, weight-averaged over energy, matches the observed direction ($219\overset{\circ}{.}2 \pm 1\overset{\circ}{.}3$, $39\overset{\circ}{.}9 \pm 2\overset{\circ}{.}3$) (Funsten et al. 2013). The center of the ribbon is found using a similar method to Funsten et al. (2013) and Zirnstein et al. (2016), which involves fitting a circle or ellipse to the peak locations of the ribbon flux.

Once the centers of the simulated ribbon are found for each energy at a particular ISMF magnitude, the centers and their uncertainties are weight-averaged over energy and circle/ellipse fit to produce the simulated ribbon weighted center. After a few iterations of the simulation and corresponding analysis, the ISMF directions required to approximately align the simulation and *IBEX* ribbon weighted centers, for a particular ISMF magnitude, are found. We emphasize that the circle/ellipse fitting is only used to find the ISMF direction that aligns the simulation and *IBEX* ribbon centers, and are not used in the analysis that finds the best-fit solution of the ISMF.

3. ANALYSIS AND RESULTS

We find that, for all values of $|\boldsymbol{B}_\infty|$, the simulated ribbon's center is located on the simulation $\boldsymbol{B}_\infty$–$\boldsymbol{V}_\infty$ plane, which is the plane defined by the LISM helium inflow ($\boldsymbol{V}_\infty$) (McComas

Table 1
LISM Boundary Conditions at 1000 AU for Each B_∞

$\lvert\boldsymbol{B}_\infty\rvert$ (μG)	2	2.5	2.75	3	3.5	4
$n_{p\infty}$ (cm^{-3})	0.11	0.1	0.095	0.09	0.08	0.07
$n_{H\infty}$ (cm^{-3})	0.165	0.1595	0.15675	0.154	0.1495	0.145
v_∞ (km s^{-1})	25.4	25.4	25.4	25.4	25.4	25.4
($\lambda_{v\infty}$, $\beta_{v\infty}$) (°)	(255.7, 5.1)	(255.7, 5.1)	(255.7, 5.1)	(255.7, 5.1)	(255.7, 5.1)	(255.7, 5.1)
T_∞ (K)	7500	7500	7500	7500	7500	7500
($\lambda_{B\infty}$, $\beta_{B\infty}$) (°)	(233.20, 29.86)	(229.61, 32.83)	(228.34, 33.81)	(226.99, 34.82)	(224.46, 36.61)	(222.31, 38.02)

Note. $n_{p\infty}$ is plasma density, $n_{H\infty}$ is neutral density, v_∞ is plasma/neutral bulk inflow speed, $\lambda_{v\infty}$ and $\beta_{v\infty}$ are longitude and latitude coordinates of the inflow direction in ecliptic J2000, and T_∞ is plasma/neutral temperature. The ISMF direction ($\lambda_{B\infty}$, $\beta_{B\infty}$) is also in ecliptic J2000 coordinates.

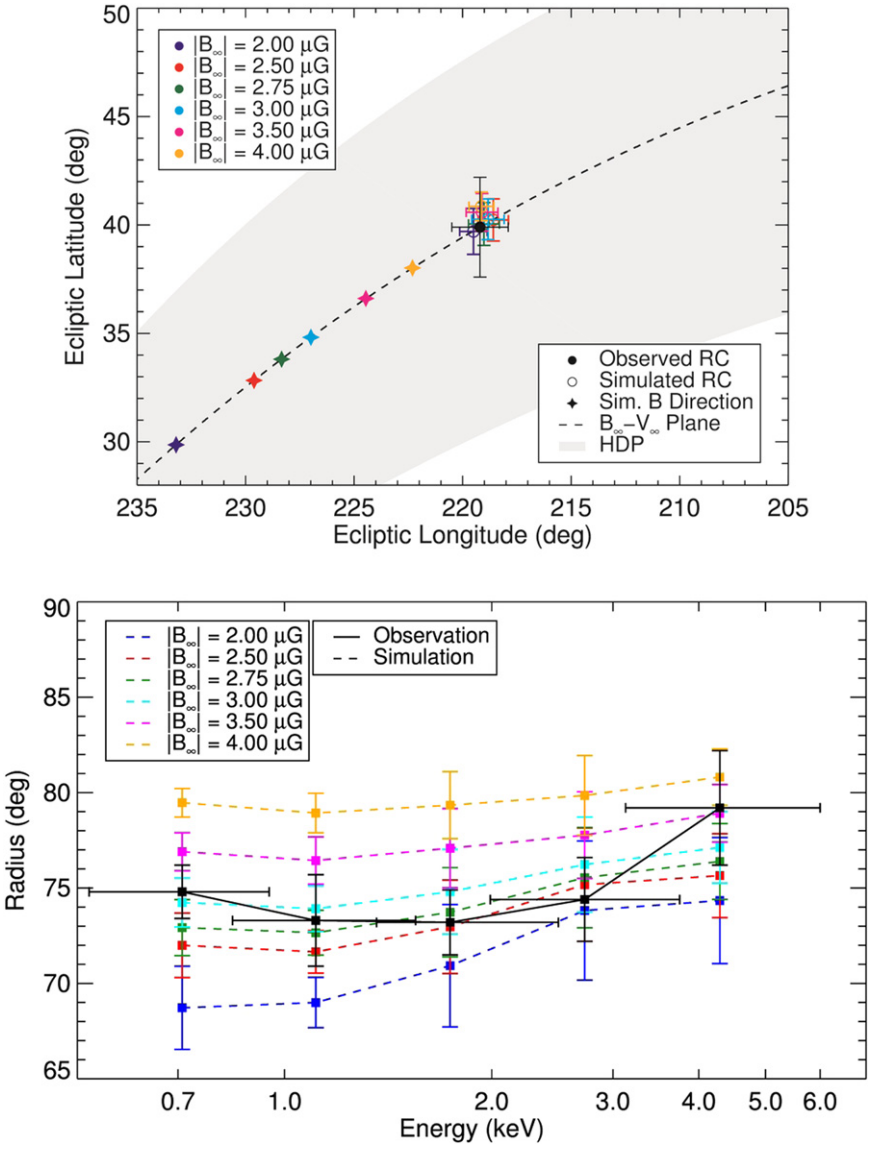

Figure 2. (Top panel) Simulated and observed ribbon centers and the corresponding ISMF. Each $\lvert\boldsymbol{B}_\infty\rvert$ requires different ISMF directions (stars) in order to produce the same ribbon center (RC) (open circles), within the uncertainty of the *IBEX* measurements (black). The centers are weighted over energy. The $\boldsymbol{B}_\infty$–$\boldsymbol{V}_\infty$ plane is shown as the black dashed curve. The hydrogen deflection plane (HDP) from Ly-alpha observations, accounting for reported uncertainties for the deflected hydrogen direction (Lallement et al. 2010), is the gray shaded region. (bottom panel) The ribbon radius (i.e., the average angular distance from the peak ribbon flux to its center) is found by fitting a circle to the simulation and *IBEX* ribbons. The *x*-axis uncertainties in the data represent the full-width half-maximum of the energy responses, which are also the same for the simulation results.

et al. 2015) and $\boldsymbol{B}_\infty$ vectors (Figure 2). A weaker $\lvert\boldsymbol{B}_\infty\rvert$ (2 μG) yields a ribbon center that is substantially offset (~15°) from $\boldsymbol{B}_\infty$, consistent with the stronger influence of hydrodynamic draping due to the Sun's motion through the LISM. Conversely, a stronger $\lvert\boldsymbol{B}_\infty\rvert$ (4 μG) yields a ribbon center offset only ~3° from $\boldsymbol{B}_\infty$, consistent with the stronger

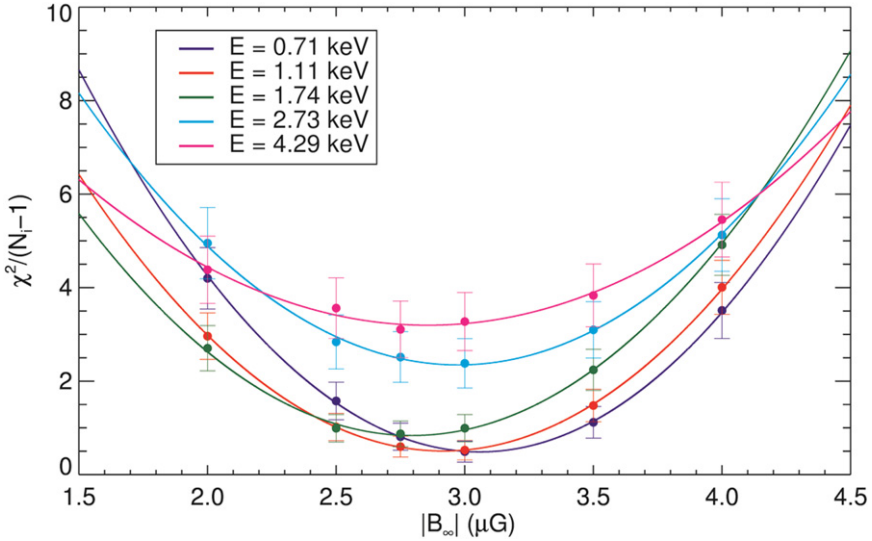

Figure 3. Quadratic fits to the reduced chi-square values computed from the comparison of the simulated and *IBEX* ribbon positions projected in the sky. The results are a function of $|\boldsymbol{B}_\infty|$ for all *IBEX*-Hi energies. N_i represents the number of data points for each energy.

influence of the ISMF on the draping geometry (Grygorczuk et al. 2011; Pogorelov et al. 2011; Heerikhuisen et al. 2014). Moreover, the $\boldsymbol{B}_\infty$–$\boldsymbol{V}_\infty$ plane shown in Figure 2 also coincides with the direction of interstellar hydrogen deflected around the heliosphere as derived from *Solar and Heliospheric Observatory*/SWAN observations of Ly-alpha background emission (Lallement et al. 2005, 2010). This supports the idea that the deflected flow of hydrogen is largely controlled by the ISMF and occurs in the $\boldsymbol{B}_\infty$–$\boldsymbol{V}_\infty$ plane (Lallement et al. 2005; Pogorelov et al. 2008a; Heerikhuisen & Pogorelov 2011).

Next, using $\boldsymbol{B}_\infty$ as a free parameter within the range shown in Figure 2, we obtain the best-fit simulated ribbon by computing the chi-square variance between the angular distances of the simulated and observed ribbons from a common ribbon center location (see Appendices). The minima of quadratic polynomial fits to the chi-square values and their uncertainties bound $\boldsymbol{B}_\infty$ over all energies (Figure 3), yielding $\sim 2.8 \leqslant |\boldsymbol{B}_\infty| \leqslant 3.1\ \mu$G. Since the ENA flux map at each energy must have a common $\boldsymbol{B}_\infty$, the best solution is found by weight-averaging the results over energy. We find a weight-averaged solution of $|\boldsymbol{B}_\infty| = 2.93 \pm 0.08\ \mu$G. The ISMF vector is found by interpolating the latitude and longitude coordinates of the simulated ISMF parameters in Figure 2 using a quadratic polynomial. This yields $(\lambda_{B\infty}, \beta_{B\infty}) = (227\overset{\circ}{.}28 \pm 0\overset{\circ}{.}69, 34\overset{\circ}{.}62 \pm 0\overset{\circ}{.}45)$, which corresponds to galactic $(25\overset{\circ}{.}98 \pm 0\overset{\circ}{.}70, 50\overset{\circ}{.}09 \pm 0\overset{\circ}{.}57)$. The angle between $\boldsymbol{B}_\infty$ and $\boldsymbol{V}_\infty$ is $\sim 39\overset{\circ}{.}5$, and the $\boldsymbol{B}_\infty$–$\boldsymbol{V}_\infty$ plane is inclined $\sim 45\overset{\circ}{.}0$ above the solar equatorial plane.

We note that the *IBEX* data at 4.29 keV may introduce a systematic uncertainty into our analysis. The significant deviation in the ribbon center and radius at this energy, which is not seen in the simulations, suggests the possibility of another source population, possibly ENAs from the inner heliosheath, which may skew our results since we excluded this source for the simulations considered here. Therefore, we performed the chi-square analysis excluding this energy, and find a best-fit ISMF of magnitude $2.94 \pm 0.09\ \mu$G, with direction $(227\overset{\circ}{.}26 \pm 0\overset{\circ}{.}71, 34\overset{\circ}{.}63 \pm 0\overset{\circ}{.}47)$. These results are very consistent with the best-fit results presented in the paper.

Table 2
Comparison of ISMF Simulation Results to *V1* Observations

	Simulation[a]	*V1*
R_{V1} (AU)	123[b]	122
$\lvert\boldsymbol{B}\rvert$ (μG)	4.8–5.6	4–6
$\lambda_{\rm RTN}$ (°)	284.6–289.4	293.0 ± 1.5[c]
$\delta_{\rm RTN}$ (°)	25.2–28.2	21.5 ± 1.5[c]

Notes. R_{V1} is the radial distance to the heliopause in the *V1* direction, and $\lambda_{\rm RTN}$ and $\delta_{\rm RTN}$ are the longitude and latitude coordinates of the ISMF in the *V1* radial–tangential–normal (RTN) spacecraft frame.
[a] The $\boldsymbol{B}$ simulation results at the location of *V1* are similar for $|\boldsymbol{B}_\infty| = 2.75$ and 3 μG. However, for accuracy, we linearly interpolate these results at 2.93 μG.
[b] The simulated heliopause has finite thickness. Thus we define the distance to the heliopause as the end of the plasma density ramp. The values for simulated $\boldsymbol{B}$ are given in ranges taken from 123 to 133 AU from the Sun (*V1* has traveled ~10 AU since crossing the heliopause).
[c] These observations are averaged from ~2012.8 to 2014.6 (Burlaga et al. 2015).

4. DISCUSSION AND CONCLUSION

Since *V1* likely exited the heliosphere in 2012 August, it has made the only in situ measurements of the ISMF (Burlaga et al. 2013). Recent measurements yield ISMF azimuthal ($\lambda_{\rm RTN}$) and elevation ($\delta_{\rm RTN}$) angles (in the *V1* RTN coordinate system) of $\lambda_{\rm RTN} = 293\overset{\circ}{.}0 \pm 1\overset{\circ}{.}5$ and $\delta_{\rm RTN} = 21\overset{\circ}{.}5 \pm 1\overset{\circ}{.}5$, and $\sim 4.0 < |\boldsymbol{B}| < 6\ \mu$G (Burlaga et al. 2015). To estimate our best-fit $\boldsymbol{B}$ at the *V1* location in our simulations, we interpolate the simulation results for $|\boldsymbol{B}_\infty| = 2.75$ and $3\ \mu$G at our best-fit value. Our simulated heliopause is consistent with *V1* measurements, and our simulation results yield ISMF values similar to the observations (Table 2). Moreover, *V1* observations confirm that the polarity of $\boldsymbol{B}_\infty$ is toward the hemisphere of the propagation of the heliosphere through the LISM. Far from the heliopause, our results predict that the ISMF approaches $|\boldsymbol{B}_\infty| \sim 2.93\ \mu$G, $\lambda_{\rm RTN} \sim 337°$, and $\delta_{\rm RTN} \sim -1°$, where the ISMF is no longer influenced by the presence of the heliosphere.

While the initial *V1* ISMF observations were surprisingly close to the Parker field orientation (Burlaga et al. 2013), it has

been shown this is a consequence of the field draping around the heliosphere (e.g., Borovikov & Pogorelov 2014) and that the *IBEX* ribbon center should be a close indicator of the ISMF (Grygorczuk et al. 2014). In fact, it was recently shown by Schwadron et al. (2015) that the direction of the ISMF observed by *V1* is evolving toward values close to the *IBEX* ribbon center as *V1* moves farther away from the heliopause. Our results generally agree with this conclusion, although we determined an offset between the ribbon center and $\boldsymbol{B}_\infty$ of $\sim 8.^\circ 3$ along the $\boldsymbol{B}_\infty$–$\boldsymbol{V}_\infty$ plane.

Lastly, our analysis uses the Heerikhuisen et al. (2010) model to simulate the ribbon. Florinski et al. (2010) suggested that the Heerikhuisen et al. model may not produce a ribbon due to efficient pitch-angle scattering of the parent ions. However, Gamayunov et al. (2010) showed that a combination of large-scale (interstellar) and small-scale (self-generated) turbulence could stabilize the ion distribution, and Summerlin et al. (2014) suggested their finite temperature could stabilize the distribution, both supporting the model. While there have been other variants of the secondary ENA mechanism (e.g., Schwadron & McComas 2013; Isenberg 2014; Giacalone & Jokipii 2015), these models produce a ribbon with highest intensity near $\boldsymbol{B}\cdot\boldsymbol{r} \sim 0$, and rely on the same draped ISMF and parent ENA distribution, which largely determines the ribbon's position. This supports the robustness of our results between other variants of the model.

This work was carried out as part of the *IBEX* mission, which is part of NASA's Explorer Program. Work at Los Alamos was performed under the auspices of the United States Department of Energy. J.H. and N.P. acknowledge support from NASA grants NNX14AJ53G, NNX14AF43G, NNX15AN72G, DOE grant DE-SC0008334, and NSF Petascale Computing Resource Allocation award OCI-1144120.

APPENDIX A
DERIVATION OF THE ISMF BY CHI-SQUARE MINIMIZATION

We find the best-fit solution using the unreduced chi-square parameter computed as the summed variances of the angular distances of the maximum ribbon flux positions r_c from the plot center, between the simulated ($r_{i,j,k}^{\rm SIM}$) and *IBEX* ($r_{i,k}^{\rm IBEX}$) ribbon at each energy and ISMF magnitude. We use *IBEX* data analyzed by Funsten et al. (2013), which consists of time weight-averaged, ram-only observations spanning 2009–2011, corrected for the Compton–Getting effect and ENA extinction as they propagate through the inner heliosphere. For a particular energy i, and ISMF case j, the chi-square parameter is computed as

$$\chi_{i,j}^2 = \sum_{k=1}^{N_i} \frac{(r_{i,k}^{\rm IBEX} - r_{i,j,k}^{\rm SIM})^2}{(\sigma_{i,k}^{\rm IBEX})^2 + (\sigma_{i,j,k}^{\rm SIM})^2},$$
$$\sigma_{i,k}^{\rm IBEX} = \begin{cases} \sigma_{i,k}^{\rm IBEX}, & \text{if } \sigma_{i,k}^{\rm IBEX} \geqslant 7^\circ/\sqrt{6} \\ 7^\circ/\sqrt{6}, & \text{if } \sigma_{i,k}^{\rm IBEX} < 7^\circ/\sqrt{6} \end{cases}, \quad (1)$$

which is summed over all azimuthal sectors accepted in the *IBEX* fitting analysis routine (see Figure 2 of Funsten et al. 2013). The uncertainty for the simulation, $\sigma_{i,j,k}^{\rm SIM}$, is the uncertainty in finding the angular distance of the ribbon from the plot center from the Gaussian function fitting. The uncertainty for the *IBEX* data, $\sigma_{i,k}^{\rm IBEX}$, is calculated in the same manner as the simulation, except that it is required to be at least $7^\circ/\sqrt{6} \approx 2.^\circ 86$, which we estimate as the 1-sigma error of the convolution of the *IBEX*-Hi hexagonal (approximately triangular) collimator and the 6° binning. The peak flux locations of the simulated ribbon are computed in the same ribbon-centered frames used for the *IBEX* data. This method takes into account any variances in the angular distance of the simulation and *IBEX* ribbon at each energy, in the same reference frame. The results of this analysis are shown in Figure 3.

Next, we find the best-fit solution for the ISMF magnitude at each energy. After computing chi-square for all ISMF cases at a particular energy using Equation (1), we fit a quadratic polynomial to the chi-square values at each energy in the form:

$$y(x) = A_0 + A_1(x - A_2)^2, \quad (2)$$

which is fit using Levenberg–Marquardt least-squares minimization, returning the best-fit parameters A_0, A_1, and A_2 and their uncertainties. The fit is weighted by the uncertainties of the chi-square values, which are found by propagating the uncertainties of each simulation and *IBEX* ribbon maximum flux location ($\sigma_{i,j,k}^{\rm SIM}$, $\sigma_{i,k}^{\rm IBEX}$) through Equation (1). The best-fit solution for the ISMF at each energy is found by the minimum value of the chi-square fit, A_2.

APPENDIX B
PROPAGATION OF UNCERTAINTIES

The best-fit ISMF magnitude for each energy i is given by the minimum chi-square in the curves shown in Figure 3. The uncertainties of the best-fit values consist of three components. First, we compute the uncertainty in the chi-square fitting using the following formula (Livadiotis 2007; Livadiotis & McComas 2013):

$$\sigma_i^{\rm chi-sqr} = \sqrt{\frac{\chi_{{\rm min},i}^2}{(N-1)A_{\rm min}}}, \quad (3)$$

where $\chi_{{\rm min},i}^2$ is the minimum (unreduced) chi-square at energy i, N_i is the number of data points at each energy i used in Equation (1), and $A_{\rm min}$ is the curvature of the chi-square fit evaluated at $\chi_{{\rm min},i}^2$, which is equal to A_1 from Equation (2).

The second component is the propagation of the uncertainties in each peak flux location ($\sigma_{i,j,k}^{\rm SIM}$, $\sigma_{i,k}^{\rm IBEX}$) used in the analysis for the simulated and *IBEX* ribbons, propagated through Equation (1), for each energy i. The total propagated uncertainty $\sigma_i^{\rm prop}$ at energy i is summed over all differences,

$$\sigma_i^{\rm prop} = \sqrt{\sum_{j=1}^{N_i} (B_i^{\rm min} - B_{i,j}^{\rm IBEX})^2 + \sum_{k=1}^{M}\sum_{j=1}^{N_i} (B_i^{\rm min} - B_{i,j,k}^{\rm SIM})^2}, \quad (4)$$

where $B_i^{\rm min}$ is the ISMF evaluated at the minimum chi-square at energy i, $B_{i,j}^{\rm IBEX}$ is the ISMF evaluated at the minimum chi-square at energy i after introducing an uncertainty in the *IBEX* data, summed over the number of azimuthal sectors N_i at energy i, and $B_{i,j,k}^{\rm SIM}$ is the ISMF evaluated at the minimum chi-square at energy i after introducing an uncertainty in the simulation results, summed over the number of azimuthal

sectors N_i, and summed over all ISMF test cases used in the chi-square fitting, $M = 6$, at each energy i.

The third component is the polynomial fit uncertainty, $\sigma_i^{\rm poly}$. This is equal to the uncertainty of $A_{\rm min} = A_2$, which is returned by the routine that solved for Equation (2). The total uncertainty for the best-fit ISMF for energy i is therefore given by

$$\sigma_i = \sqrt{(\sigma_i^{\rm chi-sqr})^2 + (\sigma_i^{\rm prop})^2 + (\sigma_i^{\rm poly})^2}\,. \quad (5)$$

APPENDIX C
COMBINING RESULTS OVER ENERGY

After deriving $B_i^{\rm min}$ and σ_i for each energy i, the combined best-fit solution is computed as the weighted mean over all energies (total = 5):

$$B_{\rm mean} = \frac{\sum_{i=1}^{5} B_i^{\rm min}/\sigma_i^2}{\sum_{i=1}^{5} 1/\sigma_i^2}. \quad (6)$$

The uncertainty of the weighted mean is a combination of the propagated uncertainty:

$$\sigma_{\rm mean}^{\rm prop} = \frac{1}{\sqrt{\sum_{i=1}^{5} 1/\sigma_i^2}}, \quad (7)$$

and the statistical uncertainty:

$$\sigma_{\rm mean}^{\rm stat} = \sqrt{\frac{\frac{1}{5}\left(\sum_{i=1}^{5} 1\Big/\sigma_i^2\right)^2}{\left(\sum_{i=1}^{5} 1\Big/\sigma_i^2\right)^2 - \sum_{i=1}^{5} 1\Big/\sigma_i^4} \frac{\sum_{i=1}^{5} (B_i^{\rm min} - B_{\rm mean})^2\Big/\sigma_i^2}{\sum_{i=1}^{5} 1\Big/\sigma_i^2}}, \quad (8)$$

which are combined to give the total uncertainty of the weighted mean:

$$\sigma_{\rm mean} = \sqrt{(\sigma_{\rm mean}^{\rm prop})^2 + (\sigma_{\rm mean}^{\rm stat})^2}\,. \quad (9)$$

The longitude and latitude coordinates of the best-fit ISMF are found by interpolating the $\boldsymbol{B}_\infty$ coordinates (separately for longitude and latitude) shown in Table 1 with a quadratic polynomial (Equation (2)) at the best-fit magnitude. Their uncertainties consist of (1) the uncertainty of the best-fit magnitude propagated through Equation (2), and (2) the polynomial fit uncertainty, i.e., the uncertainty of A_2 in Equation (2).

REFERENCES

Ben-Jaffel, L., & Ratkiewicz, R. 2012, A&A, 546, A78
Ben-Jaffel, L., Strumik, M., Ratkiewicz, R., & Grygorczuk, J. 2013, ApJ, 779, 130
Borovikov, S. N., & Pogorelov, N. V. 2014, ApJL, 783, L16
Burlaga, L. F., Florinski, V., & Ness, N. F. 2015, ApJL, 804, L31
Burlaga, L. F., Ness, N. F., & Stone, E. C. 2013, Sci, 341, 147
Bzowski, M., Möbius, E., Tarnopolski, S., Izmodenov, V., & Gloeckler, G. 2009, SSRv, 143, 177
Florinski, V., Zank, G. P., Heerikhuisen, J., Hu, Q., & Khazanov, I. 2010, ApJ, 719, 1097
Funsten, H. O., Allegrini, F., Bochsler, P., et al. 2009b, SSRv, 146, 75
Funsten, H. O., Allegrini, F., Crew, G. B., et al. 2009a, Sci, 326, 964
Funsten, H. O., DeMajistre, R., Frisch, P. C., et al. 2013, ApJ, 776, 30
Gamayunov, K., Zhang, M., & Rassoul, H. 2010, ApJ, 725, 2251
Giacalone, J., & Jokipii, J. R. 2015, ApJL, 812, L9
Grygorczuk, J., Czechowski, A., & Grzedzielski, S. 2014, ApJL, 789, L43
Grygorczuk, J., Ratkiewicz, R., Strumik, M., & Grzedzielski, S. 2011, ApJL, 727, L48
Heerikhuisen, J., & Pogorelov, N. 2010, in ASP Conf. Ser. 429, Numerical Modeling of Space Plasma Flows, ed. N. V. Pogorelov, E. Audit, & G. P. Zank (San Francisco, CA: ASP), 227
Heerikhuisen, J., & Pogorelov, N. V. 2011, ApJ, 738, 29
Heerikhuisen, J., Pogorelov, N. V., Zank, G. P., et al. 2010, ApJL, 708, L126
Heerikhuisen, J., Zirnstein, E. J., Funsten, H. O., Pogorelov, N. V., & Zank, G. P. 2014, ApJ, 784, 73
Isenberg, P. A. 2014, ApJ, 787, 76
Izmodenov, V. V., Alexashov, D. B., & Ruderman, M. S. 2014, ApJL, 795, L7
Izmodenov, V. V., Malama, Y. G., Ruderman, M. S., et al. 2009, SSRv, 146, 329
Lallement, R., Quémerais, E., Bertaux, J. L., et al. 2005, Sci, 307, 1447
Lallement, R., Quémerais, E., Koutroumpa, D., et al. 2010, in AIP Conf. Ser. 1216, Twelfth Int. Solar Wind Conf., ed. M. Maksimovic, K. Issautier, N. Meyer-Vernet, M. Moncuquet, & F. Pantellini (Melville, NY: AIP), 555
Livadiotis, G. 2007, PhyA, 375, 518
Livadiotis, G., & McComas, D. J. 2013, JGRA, 118, 2863
Malama, Y. G., Izmodenov, V. V., & Chalov, S. V. 2006, A&A, 445, 693
McComas, D. J., Allegrini, F., Bochsler, P., et al. 2009a, SSRv, 146, 11
McComas, D. J., Allegrini, F., Bochsler, P., et al. 2009b, Sci, 326, 959
McComas, D. J., Bzowski, M., Fuselier, S. A., et al. 2015, ApJS, 220, 22
Opher, M., Bibi, F. A., Toth, G., et al. 2009, Natur, 462, 1036
Parker, E. N. 1961, ApJ, 134, 20
Pogorelov, N. V., Heerikhuisen, J., & Zank, G. P. 2008a, ApJL, 675, L41
Pogorelov, N. V., Heerikhuisen, J., Zank, G. P., et al. 2011, ApJ, 742, 104
Pogorelov, N. V., Suess, S. T., Borovikov, S. N., et al. 2013, ApJ, 772, 2
Pogorelov, N. V., Zank, G. P., Borovikov, S. N., et al. 2008b, in ASP Conf. Ser. 385, Numerical Modeling of Space Plasma Flows, ed. N. V. Pogorelov, E. Audit, & G. P. Zank (San Francisco CA: ASP), 180
Ratkiewicz, R., & Grygorczuk, J. 2008, GeoRL, 35, L23105
Ratkiewicz, R., Strumik, M., & Grygorczuk, J. 2012, ApJ, 756, 3
Schwadron, N. A., Bzowski, M., Crew, G. B., et al. 2009b, Sci, 326, 966
Schwadron, N. A., Crew, G., Vanderspek, R., et al. 2009a, SSRv, 146, 207
Schwadron, N. A., & McComas, D. J. 2013, ApJ, 764, 92
Schwadron, N. A., Richardson, J. D., Burlaga, L. F., McComas, D. J., & Moebius, E. 2015, ApJL, 813, L20
Sokół, J. M., Bzowski, M., Tokumaru, M., Fujiki, K., & McComas, D. J. 2013, SoPh, 285, 167
Stone, E. C., Cummings, A. C., McDonald, F. B., et al. 2005, Sci, 309, 2017
Stone, E. C., Cummings, A. C., McDonald, F. B., et al. 2008, Natur, 454, 71
Strumik, M., Ben-Jaffel, L., Ratkiewicz, R., & Grygorczuk, J. 2011, ApJL, 741, L6
Summerlin, E. J., Viñas, A. F., Moore, T. E., Christian, E. R., & Cooper, J. F. 2014, ApJ, 793, 93
Zank, G. P., Heerikhuisen, J., Wood, B. E., et al. 2013, ApJ, 763, 20
Zirnstein, E. J., Funsten, H. O., Heerikhuisen, J., & McComas, D. J. 2016, A&A, 586, A31
Zirnstein, E. J., Heerikhuisen, J., & McComas, D. J. 2015, ApJL, 804, L22
Zirnstein, E. J., Heerikhuisen, J., McComas, D. J., & Schwadron, N. A. 2013, ApJ, 778, 112